



Rapid and highly sensitive detection of formaldehyde gas via a polyoxometalate–CuBi₂O₄ composite gas sensor

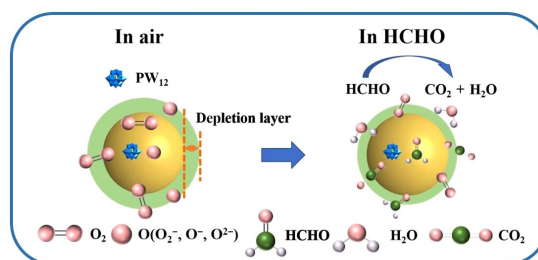
Pinfan Song, Ying Yang, Feng Li, Hui Yu, Xiangting Dong, and Tianqi Wang  

Key Laboratory of Applied Chemistry and Nanotechnology at Universities of Jilin Province, School of Chemistry and Environmental Engineering, Changchun University of Science and Technology, Changchun 130022, China

 Cite This: *Polyoxometalates*, 2024, 3, 9140053

 Read Online

ABSTRACT: Quick response and high sensitivity are equally important for the practical application of gas sensors. In this study, we introduced polyoxometalates (POMs) into a classical ternary metal oxide CuBi₂O₄ for the first time by convenient electrospinning and prepared a group of heater-type gas sensors by using CuBi₂O₄/PW₁₂ composite nanofibers. The sensor performances to formaldehyde gas were explored. The results proved that the gas-sensing response of the CuBi₂O₄/PW₁₂ (PW₁₂ = H₃PW₁₂O₄₀·xH₂O) composite sensor to 100 ppm formaldehyde gas was increased to 6.68, which was 3.92 times greater than the sensing capacity of the pure CuBi₂O₄ sensor. Simultaneously, the sensor exhibited a highly rapid response/recovery time of only 1/2 s, which is significantly faster than performances of CuBi₂O₄ gas sensors reported in the past literature. The cause of the improvement of the sensing performance was assessed via mechanism study, and it was found that the introduction of PW₁₂ into the sensor contributed to its enhanced performance. It was found that PW₁₂, as an electron acceptor, increased carrier mobility and reduced electron–hole recombination, thus contributing to enhanced gas-sensing properties. Moreover, other gas-sensing parameters such as selectivity, humidity resistance, repeatability, long-term stability were investigated. Hence, this study contributed to the literature on the development of polyoxometalates-based gas sensors.



KEYWORDS: CuBi₂O₄, polyoxometalates, polyoxotungstate, gas sensing, formaldehyde

1 Introduction

Due to the impact of energy crisis and air pollution, we urgently need harmful gas detection technology to ensure the health of the people and environment [1–5]. Formaldehyde is a recognized toxic gas; it has carcinogenic effects, and is strongly harmful to the human respiratory system, liver function, etc. Therefore, monitoring the existence of formaldehyde content in the environment is of critical importance. In recent years, metal oxide gas-sensing semiconductors have been used for detecting formaldehyde, and gas sensors constructed with such semiconductor materials have been continually explored [6–8]. However, as the existing formaldehyde gas sensors have the shortcomings of low gas response and poor selectivity [9], researchers have been exploring the development of new gas-sensing semiconductors.

Ternary metal oxides (LaFeO₃ [10], CuFe₂O₄ [11], etc.) can be used as gas-sensing materials due to their structural and compositional diversity. Among these, CuBi₂O₄ is a p-type semiconductor with a narrow band gap and a low conduction band


position [12]. Therefore, it is often used as a photocatalyst to produce hydrogen in water and as a photocathode for the study of photoelectrochemical properties; it has also been developed as a core material in gas sensors [13–15]. Because of the rapid electron–hole recombination of pure CuBi₂O₄, the sensitivity of CuBi₂O₄-based gas sensors continues to be less than ideal. Therefore, to improve the sensitivity of these sensors, the construction of composite materials is being undertaken by researchers.

Polyoxometalates (POMs) are a series of inorganic metal-oxo cluster compounds dominated by transition metal elements (Mo, W, V, etc.). They have diverse structures and can be acquired by condensing inorganic acids [16–18]. POMs are not only low cost and easy to use, but are also widely used in many fields including catalysis, coordination chemistry, molecular-based functional materials, and lithium-sulfur batteries [19–24]. Furthermore, many studies on POMs in gas sensors have been reported. This is because POMs are able to trap electrons from semiconductors and effectively transport them. This ability allows POMs to act as electron acceptors in traditional semiconductors, thus reducing the recombination between electrons and holes and thereby improving sensing capabilities. However, the gas-sensitive properties of the POM-modified CuBi₂O₄ composite have not yet been explored in the existing literature.

In this study, we synthesized phosphotungstic acid

Received: October 9, 2023; **Revised:** December 23, 2023

Accepted: January 2, 2024

 Address correspondence to wangtq302@cust.edu.cn



清华大学出版社
Tsinghua University Press

SciOpen

<https://doi.org/10.26599/POM.2024.9140053>

Polyoxometalates, 2024, 3, 9140053

($H_3PW_{12}O_{40} \cdot xH_2O$, PW_{12}) doped $CuBi_2O_4$ one-dimensional nanofibers by using electrospinning technology and characterized their composition and morphology. The $CuBi_2O_4/PW_{12}$ composite nanofibers were used to construct heater-type gas sensors, and were used to detect formaldehyde gas in air. At an appropriate operating temperature, it was found that the sensitivity response of the $CuBi_2O_4/3\%PW_{12}$ sensor to formaldehyde gas was enhanced by 3.92 times as compared with that of the pure $CuBi_2O_4$ sensor. The sensor also exhibited a highly rapid response/recovery time of only 1/2 s. Moreover, other gas-sensing parameters such as selectivity, humidity resistance, repeatability, long-term stability of the sensors were comprehensively investigated. In the mechanism study, the enhancement of gas sensitivity of $CuBi_2O_4/3\%PW_{12}$ sensor could be attributed to the introduction of PW_{12} , that works as electron acceptors and separate electrons and holes. Hence, this study is meaningful for developing POM-based gas sensors.

2 Materials and methods

2.1 Materials

Phosphotungstic acid ($H_3PW_{12}O_{40} \cdot xH_2O$ (PW_{12}), $M_w = 2880.3$), $Bi(NO_3)_3 \cdot 5H_2O$, $Cu(NO_3)_2 \cdot 3H_2O$, N,N-dimethylformamide (DMF, $\geq 99.5\%$), acetic acid (CH_3COOH , $\geq 99.5\%$), and polyvinylpyrrolidone (PVP, $M_w = 1,300,000$) were purchased from Aladdin industrial Co. Ltd. The reagents used were both of AR grade.

2.2 Synthesis of nanofibers

According to Refs. [25, 26], $CuBi_2O_4/PW_{12}$ composite nanofibers were synthesized via electrospinning technology. Briefly, in an experimental environment with a temperature of 25 °C and a humidity of 25% RH, 1.7 g of PVP was dissolved in 8.0 mL of DMF; another 2.5 mL of acetic acid (HAC) was added to this to obtain a homogeneous solution. Subsequently, 0.8 g $Bi(NO_3)_3 \cdot 5H_2O$, 0.2 g $Cu(NO_3)_2 \cdot 3H_2O$, and PW_{12} of appropriate mass were added to the mixed solution, and the mass fractions of PW_{12} were 1%, 3%, 5%, and 10%, respectively. The mixture was stirred for 12 h to obtain a blue spinning solution; the spinning solution was transferred to a 20.0 mL syringe and electrospun with a stainless steel needle as the anode and barbed wire as the cathode. During electrospinning, the distance from the tip of the needle to the cathode is approximately 15 cm and the voltage is approximately 16 kV. After electrospinning, the precursor nanofibers were calcined in an oxidation oven at 500 °C. The heating rate was set to 1 °C/min and annealed for 2 h. When the sample was naturally cooled to room temperature, $CuBi_2O_4/PW_{12}$ composite nanofibers were obtained. The same method was used to synthesize pure $CuBi_2O_4$ nanofibers without PW_{12} . In this study, $CuBi_2O_4/PW_{12}$ nanofibers with different PW_{12} contents were expressed as $CuBi_2O_4/x\%PW_{12}$ ($x = 0, 1, 3, 5, \text{ and } 10$).

2.3 Characterization of nanofibers

X-ray diffraction (XRD) analyses were performed with a Rigaku D/max200PC X-ray diffractometer, using $CuK\alpha 1$ radiation ($\lambda = 1.5405 \text{ \AA}$). Field-emission scanning electron microscopy (SEM) was performed with a Hitachi S-4800 FEG-SEM equipped with energy-dispersive X-ray spectroscopy (EDS) analysis. Fourier transform infrared spectroscopy (FT-IR) spectra were recorded on a Nicolet Impact 410 FT-IR spectrometer. ultraviolet–visible (UV–vis) diffuse reflectance spectroscopy analyses were performed using a Varian

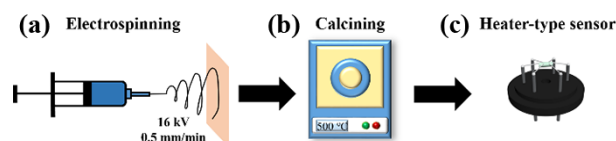


Figure 1 (a) Schematic of the electrospinning device, (b) oxidation calcination, and (c) heater-type sensor.

Cary 500 instrument. X-ray photoelectron spectroscopy (XPS) analyses were performed using a Thermo ESCALAB 250 instrument. Photoluminescence (PL) spectra were recorded using a fluorescence spectrophotometer (Edinburgh Instruments, FLSP-920). Electrochemical impedance spectroscopy (EIS) was performed in an aqueous solution of 0.1 M Na_2SO_4 exposed to air.

2.4 Gas-sensing measurement

The prepared sample was ground into powder with a mortar; an appropriate amount of ethanol was added and stirred to form a slurry; finally, a small-sized brush was applied to an alumina ceramic tube with a gold electrode. The device was subsequently aged in an oven at 80 °C for 24 h. Gas-sensing performance testing was performed using a Tektronix DMM 4040-digit precision multimeter. The sensing performance was tested at different temperatures. During the test, a certain amount of formaldehyde gas was injected into the chamber with dry air as the background gas, and it was observed that the resistance changed from the original resistance (R_a) in the air to the new stable resistance (R_g) in the target gas. This change in resistance used to calculate the gas-sensitive response value (S) of the gas was as follows

$$S = R_g/R_a \times 100\% \quad (1)$$

When testing the selectivity of the sensor, for the oxidizing gas NO_2 , pure NO_2 mixed with air was used as the target gas, and other target gases were prepared by mixing a certain amount of liquid and air. In the humidity test, saturated inorganic salt solutions with different amounts of saturated steam were used to prepare gas samples with different humidity levels. The relationship between saturated inorganic salt solution and humidity was as follows: LiCl (11%), $MgCl_2$ (32.8%), K_2CO_3 (43%), $Mg(NO_3)_2$ (54.3%), NaCl (67%), $CuCl_2$ (75.3%), KCl (85%), KNO_3 (93.5%).

3 Results and discussion

3.1 Morphologies and structures

To analyze the composition, morphology, and structure of the samples, SEM images were obtained. Figure 2 shows SEM images and EDS test results of composite materials at different magnifications. Figures 2(a)–2(e) shows SEM images of $CuBi_2O_4/x\%PW_{12}$ ($x = 0, 1, 3, 5, \text{ and } 10$). The image results showed that the samples were fibrous and had a diameter of approximately 200 nm. The morphology of the sample was relatively uniform. This showed that the composite material maintained the fiber structure of pure $CuBi_2O_4$ and that the introduced PW_{12} did not destroy the structure of the original $CuBi_2O_4$. To compare the stability of the sample topography before and after the experiment, we also measured the SEM of $CuBi_2O_4/3\%PW_{12}$ after the experiment, as shown in Fig. 2(g). Due to the influence of grinding, the fiber fracture after the experiment was more pronounced. Figures 2(i)–2(l) show the EDS images of $CuBi_2O_4/3\%PW_{12}$

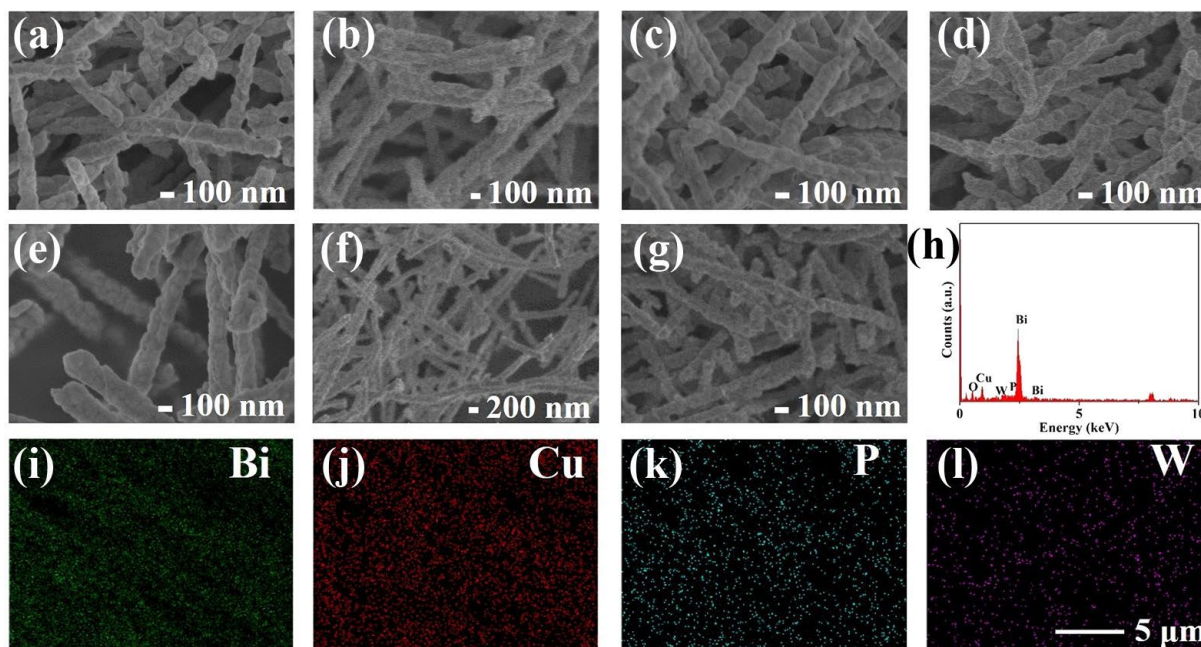


Figure 2 (a)–(e) SEM images of $\text{CuBi}_2\text{O}_4/x\%\text{PW}_{12}$ ($x = 0, 1, 3, 5,$ and 10). SEM images of (f) CuBi_2O_4 and (g) $\text{CuBi}_2\text{O}_4/3\%\text{PW}_{12}$ after the experiment. (h) EDS pattern of $\text{CuBi}_2\text{O}_4/3\%\text{PW}_{12}$ and (i)–(l) the corresponding EDS mappings of Bi, Cu, P, and W elements.

composite nanofiber. According to the EDS images, the elements Bi, Cu, P, and W were evenly distributed. **Figure 2(h)** also shows the mapping of elements in $\text{CuBi}_2\text{O}_4/3\%\text{PW}_{12}$ composite nanofibers, indicating that PW_{12} was uniformly distributed in the composite.

To determine the structure and crystal phase of $\text{CuBi}_2\text{O}_4/x\%\text{PW}_{12}$ and CuBi_2O_4 composite nanofibers, we performed experiments using an X-ray powder diffractometer. The XRD spectra of the nanofibers are displayed in **Fig. 3(a)**. All samples had characteristic diffraction peaks at 2θ of $20.8^\circ, 27.9^\circ, 32.4^\circ, 45.9^\circ, 46.6^\circ,$ and 55.6° , corresponding to the (200), (211), (102), (312), (411), and (332) crystal planes of CuBi_2O_4 (JCPDS NO. 48-1886). Additionally, there was no difference between the XRD of $\text{CuBi}_2\text{O}_4/3\%\text{PW}_{12}$ after and before the experiment. However, because of the poor content or the amorphous state of PW_{12} , the diffraction peak of PW_{12} was not evident in the XRD spectra. As displayed in **Fig. 3(b)**, the FT-IR spectra of $\text{CuBi}_2\text{O}_4/x\%\text{PW}_{12}$ exhibited absorption peaks at $802\text{--}1109\text{ cm}^{-1}$ compared with the infrared spectrum of pure CuBi_2O_4 . The peaks of P–O, W=O, W–O, and W–O–W corresponded to the four characteristic peaks of $802, 897, 994,$ and 1109 cm^{-1} in the spectrum, respectively. This was consistent with the position of the PW_{12} absorption peak reported in Ref. [27]. This showed that after high-temperature

calcination, the Keggin-type structural skeleton of PW_{12} continued to be retained in the target sample. Additionally, we also studied the effect of PW_{12} on CuBi_2O_4 by using the Raman spectrum. In **Fig. 3(c)**, we can observe the Raman bands of CuBi_2O_4 around $75, 122, 184, 254, 388,$ and 568 cm^{-1} , which are close to the Raman peaks recorded in Ref. [28]. The Raman band at 914 cm^{-1} was produced by the introduction of PW_{12} . Thus, the results proved the existence of PW_{12} , and showed that we successfully synthesized $\text{CuBi}_2\text{O}_4/x\%\text{PW}_{12}$ composite nanofibers.

To further determine the chemical composition of $\text{CuBi}_2\text{O}_4/3\%\text{PW}_{12}$ nanomaterials, we measured the XPS of $\text{CuBi}_2\text{O}_4/3\%\text{PW}_{12}$. **Figure 4(a)** shows the full scan spectrum of Cu, Bi, O, C, P, and W elements. The C element was present due to the organic oil in the test instrument. **Figures 4(b)–4(f)** show the high-resolution XPS spectra of Cu 2p, Bi 4f, P 2p, W 4f, and O 1s. The XPS data further validated the introduction of PW_{12} in CuBi_2O_4 nanofibers.

EIS testing can visually show the separation efficiency of the charge and transfer resistances [29]. The arc in the Nyquist diagram [30] shows that the larger the radius of the arc, the greater the charge transfer resistance. The Nyquist plot can be fitted to the equivalent circuit shown in **Fig. 5(a)**. In this equivalent circuit, $R_s, R_{ct},$ and CPE represent the solution resistance, charge transfer resistance across the interface of semiconductor||electrolyte, and

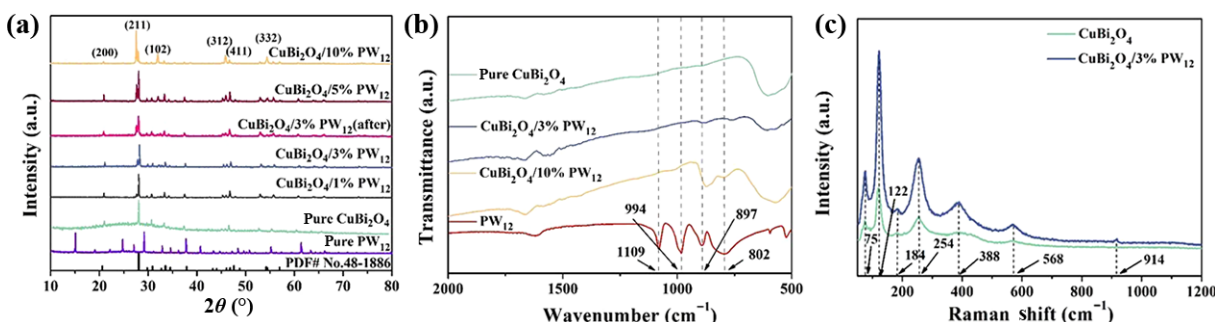


Figure 3 (a) XRD patterns, (b) FT-IR spectra, and (c) Raman spectra of CuBi_2O_4 and $\text{CuBi}_2\text{O}_4/x\%\text{PW}_{12}$.

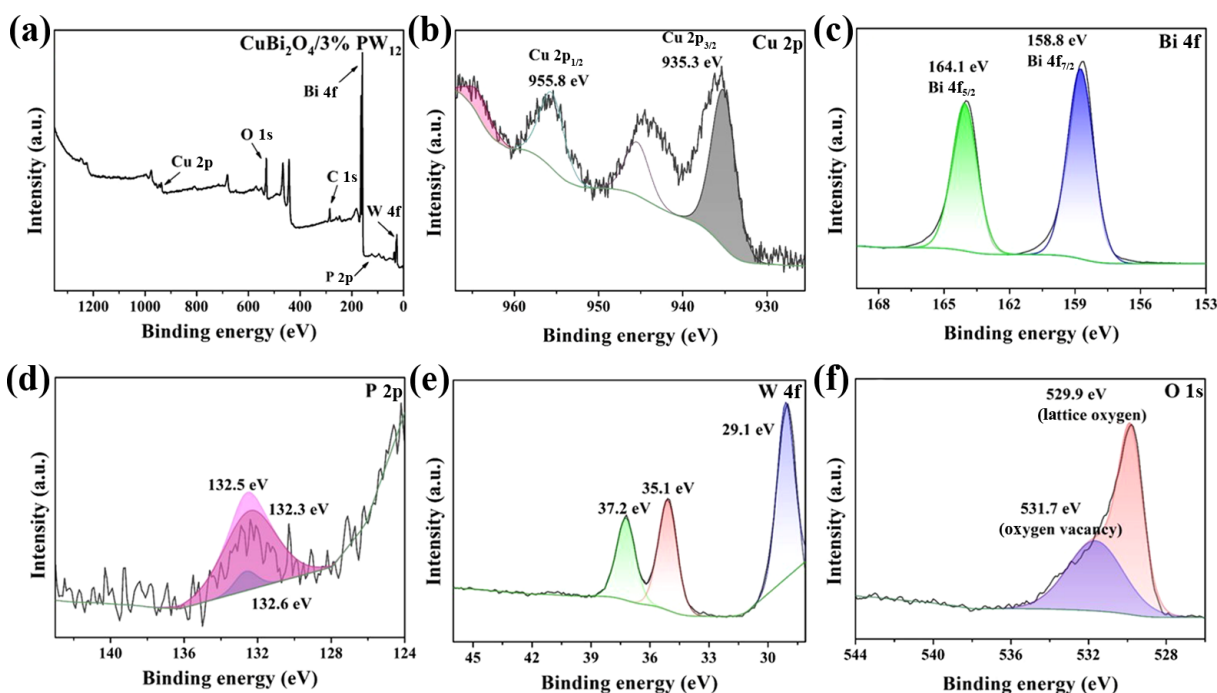


Figure 4 (a) XPS spectrum of $\text{CuBi}_2\text{O}_4/3\%\text{PW}_{12}$ and high-resolution XPS spectra: (b) Cu 2p, (c) Bi 4f, (d) P 2p, (e) W 4f, and (f) O 1s.

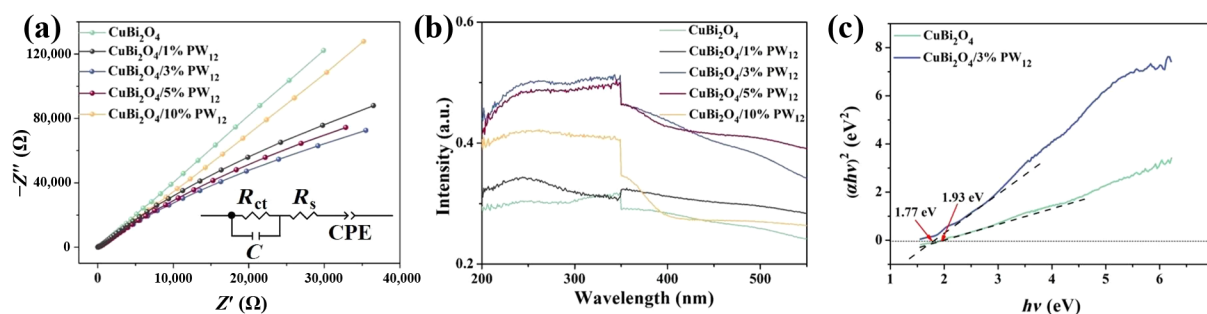


Figure 5 (a) Nyquist plots and UV-vis absorption diffuse reflectance spectra of CuBi_2O_4 and $\text{CuBi}_2\text{O}_4/x\%\text{PW}_{12}$. (c) $(\alpha h\nu)^2$ vs. $h\nu$ plots of CuBi_2O_4 and $\text{CuBi}_2\text{O}_4/3\%\text{PW}_{12}$.

constant phase element for the semiconductor|electrolyte interface, respectively [31]. Among them, the R_s value was 8.625Ω , and the R_{ct} fitting values of CuBi_2O_4 and $\text{CuBi}_2\text{O}_4/3\%\text{PW}_{12}$ were 5.314 and 1.072Ω , respectively. Because the fitted R_{ct} value of $\text{CuBi}_2\text{O}_4/3\%\text{PW}_{12}$ approximately was five times smaller than that of the original CuBi_2O_4 , the $\text{CuBi}_2\text{O}_4/3\%\text{PW}_{12}$ composite proved to have better charge transfer efficiency. As an electron acceptor, PW_{12} can improve the electron transport efficiency in CuBi_2O_4 and effectively inhibit the recombination of electron-hole pairs. The results showed that the $\text{CuBi}_2\text{O}_4/x\%\text{PW}_{12}$ composites had good properties and were suitable for the preparation of gas sensors. Figure 5(b) shows the UV-Vis diffuse reflectance spectra of CuBi_2O_4 and $\text{CuBi}_2\text{O}_4/x\%\text{PW}_{12}$. We observed that $\text{CuBi}_2\text{O}_4/x\%\text{PW}_{12}$ materials have significant absorption in the UV region. Additionally, Fig. 5(c) shows the band gap energies of pure CuBi_2O_4 and $\text{CuBi}_2\text{O}_4/3\%\text{PW}_{12}$. The E_g values of CuBi_2O_4 and $\text{CuBi}_2\text{O}_4/3\%\text{PW}_{12}$ were estimated to be 1.93 and 1.77 eV, respectively. The band gap results showed that the addition of PW_{12} reduced the band gap of CuBi_2O_4 and improved the gas-sensing performance.

3.2 Gas-sensing performance

First, we tested the sensing responses of $\text{CuBi}_2\text{O}_4/x\%\text{PW}_{12}$ sensors to 100 ppm formaldehyde gas from 370 to 470 °C. As displayed in

Fig. 6(a), when the temperature increased, the response values of each sensor showed a trend of first increasing and subsequently decreasing. At 410 °C, the response value of $\text{CuBi}_2\text{O}_4/3\%\text{PW}_{12}$ sensor was the highest, being 3.92 times greater than that of the pure CuBi_2O_4 sensor. This showed that the optimal content of PW_{12} in the sensor was 3%. Changing the temperature affected the number of electron-hole pairs in the material and the rate of gas adsorption/desorption. At low temperatures, the number of electron-hole pairs was small, the electron mobility was low, and the response value of the sensor was limited. When the temperature reached 410 °C, the response value reached its peak. However, when the temperature exceeded 410 °C, the high temperature accelerated the desorption of the gas; therefore, the sensitivity response of the sensor decreased. The R_a values of each sample at different temperatures are shown in Fig. 6(e). It was observed that R_a gradually decreased as the temperature increased. The change of R_a may be due to the introduction of the right amount of PW_{12} electron acceptor, resulting in a decrease in resistance. However, a higher amount of addition of PW_{12} may lead to high resistance.

To determine the gas selectivity of the sensor, we measured the responses of the sensor to 100 ppm formaldehyde, toluene, ethanol, acetone, ammonia, and nitrogen dioxide gases. Figure 6(b) shows that all $\text{CuBi}_2\text{O}_4/x\%\text{PW}_{12}$ sensors had the highest response to

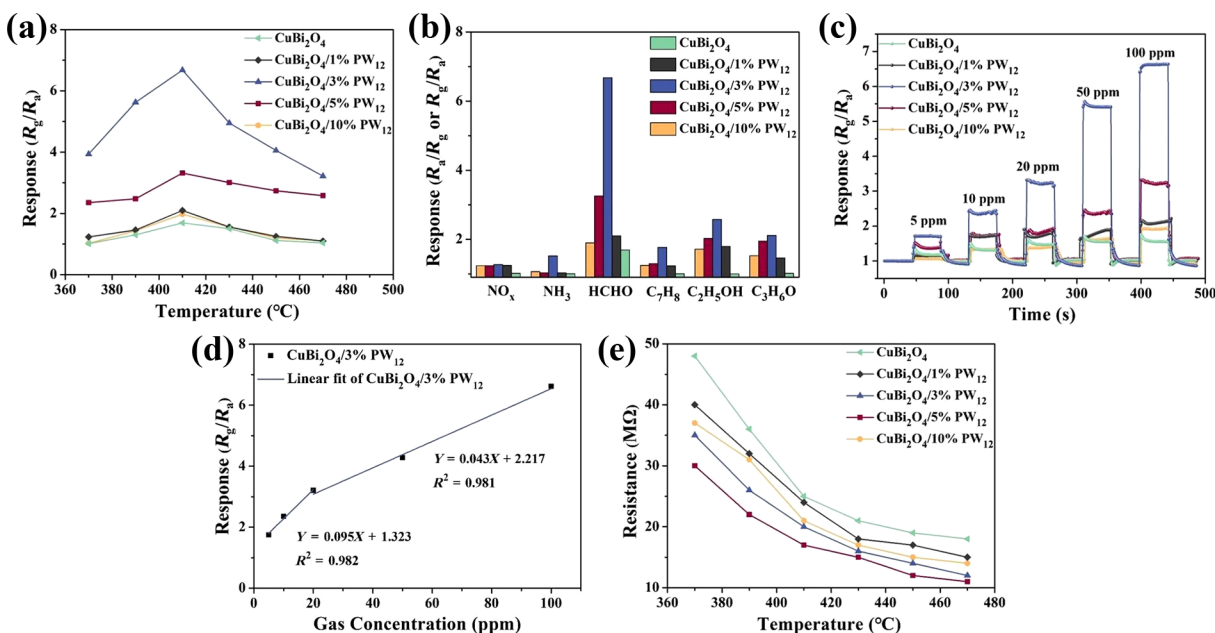


Figure 6 (a) Response values of CuBi₂O₄/x%PW₁₂ sensors for 100 ppm formaldehyde at different operating temperatures. (b) Selectivity of CuBi₂O₄/x%PW₁₂ sensors for 100 ppm of various gases. (c) Dynamic response/recovery curves of CuBi₂O₄/x%PW₁₂ sensors for 5–100 ppm formaldehyde. (d) Response values of CuBi₂O₄/3%PW₁₂ sensor and formaldehyde concentration linear fitting curve. (e) R_a of CuBi₂O₄/x%PW₁₂ sensors at different temperatures.

formaldehyde gas, and that they had a low response to all remaining gases. This showed that the CuBi₂O₄/x%PW₁₂ sensor exhibited high selectivity for formaldehyde gas. The response of CuBi₂O₄/3%PW₁₂ sensors to formaldehyde gas continued to be the highest. Figure 6(c) shows the responses of the CuBi₂O₄/x%PW₁₂ sensors to 5–100-ppm formaldehyde gas at an optimal temperature. The results showed that while the concentration increased, the response value of the sensor also increased, and that the response value of CuBi₂O₄/3%PW₁₂ sensor increased more obviously. Figure 6(d) shows the linear fitting curve of the CuBi₂O₄/3%PW₁₂ sensor response value to the formaldehyde concentration. The linear relationship between CuBi₂O₄/3%PW₁₂ sensor response value and formaldehyde concentration was evaluated by R^2 . When the CuBi₂O₄/3%PW₁₂ sensor was tested in 5–20 ppm formaldehyde, because of the low gas concentration, it could not fully occupy the adsorption site in the material; hence, its response time was faster. Therefore, in 5–20 ppm formaldehyde gas, the linear relationship of R^2 value of 0.982 was conformed. As the gas concentration increased, it took more time for the gas to occupy a deeper adsorption site in the material. Subsequently, the CuBi₂O₄/3%PW₁₂ sensor conformed to a linear relationship with an R^2 value of 0.981 in 20–100 ppm gas. This result provides a reliable basis for determining the detection range of CuBi₂O₄/3%PW₁₂ sensors. Additionally, because of the linear fitting equation, the limit of detection (LOD) of the CuBi₂O₄/3%PW₁₂ sensor was calculated to be 218 ppb.

To observe when the response value of the CuBi₂O₄/x%PW₁₂ sensor changed in formaldehyde gas, we tested the response and recovery time (t_{res} and t_{rec}) of the sensors to 100 ppm formaldehyde. The experimental results are shown in Fig. 7. Compared with the original CuBi₂O₄ sensor, the $t_{\text{res}}/t_{\text{rec}}$ of the CuBi₂O₄/3%PW₁₂ sensor increased from 5/10 to 1/2 s. The $t_{\text{res}}/t_{\text{rec}}$ of other sensors with PW₁₂ content was also significantly higher. Therefore, it can be concluded that adding 3%PW₁₂ can not only improve the response of the sensor, but also results in the sensor having the fastest response and

recovery speed. Additionally, we can also see from Fig. 7 that the R_a value of the sensors did not fluctuate significantly before filling with formaldehyde gas. This result showed that the resistance of the CuBi₂O₄/x%PW₁₂ sensor was relatively stable during the test.

A comparison of CuBi₂O₄ gas sensors in the literatures is displayed in Table 1. This information shows that the target gases of CuBi₂O₄ and CuBi₂O₄-based sensors are regular volatile organic compounds (VOCs) (ethanol and formaldehyde). Compared with other CuBi₂O₄ materials, the CuBi₂O₄/PW₁₂ nanofibers synthesized in this study exhibited the same level of response. Significantly, the response/recovery time of the CuBi₂O₄/3%PW₁₂ was significantly faster than that reported in the literature. This can be attributed to the fact that the presence of POMs reduced the recombination between electrons and holes and the one-dimensional structure was beneficial for the rapid transfer of electrons.

Additionally, other sensing parameters of the CuBi₂O₄/x%PW₁₂ sensor were analyzed in detail. Figure 8(a) shows the relative humidity resistance test of the CuBi₂O₄/3%PW₁₂ sensor. During the varying humidity conditions, the response of the sensor tended to decline. When the humidity was up to 93.5%, the response value was 3.7. This showed that humidity had an evident influence on the sensor. When we performed repeatable experiments on the CuBi₂O₄/3%PW₁₂ sensor (Fig. 8(b)), we found that the response was stable within six cycles; this indicated that the sensor had good repeatability for formaldehyde at 410 $^{\circ}\text{C}$. To explore the stability of the sensor, we tested the response of the CuBi₂O₄/3%PW₁₂ sensor over 30 days. As displayed in Fig. 8(c), the response value decreased slightly, but remained largely unchanged.

3.3 Mechanism research

To analyze in detail how the introduction of PW₁₂ affects the gas-sensing performance of CuBi₂O₄, we discussed the gas-sensing mechanism of the CuBi₂O₄/x%PW₁₂ sensor by using fluorescence emission spectroscopy (excitation wavelength of 254 nm). As shown by the PL spectra (Fig. 9), it was observed that the composite

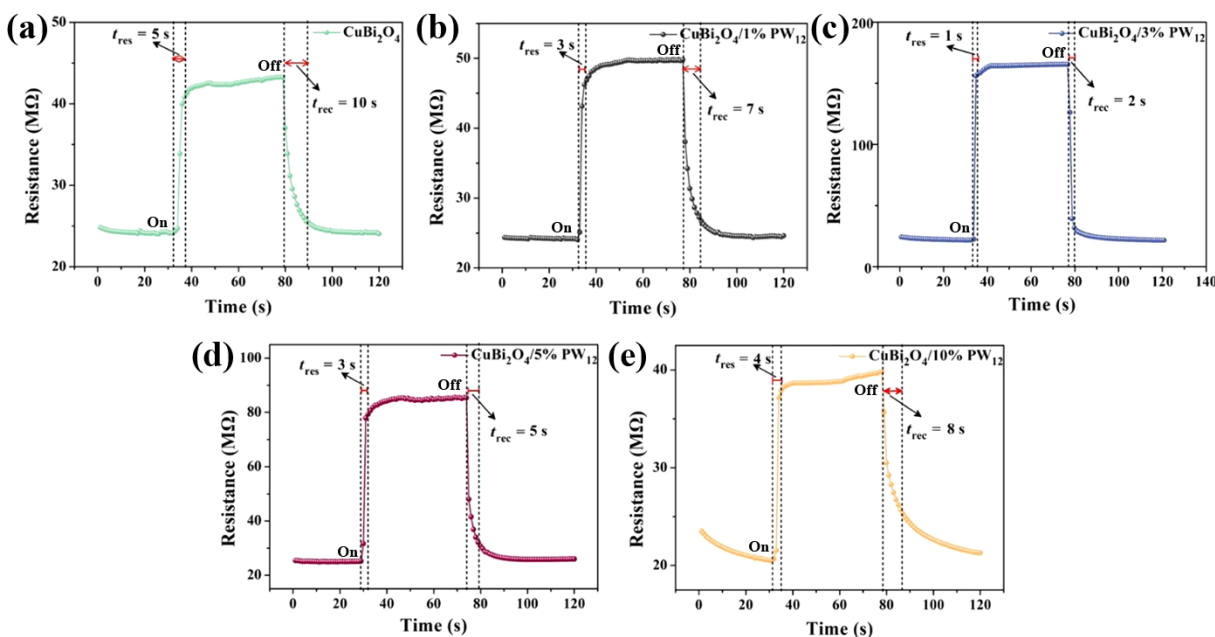


Figure 7 (a)–(e) Resistance–response and recovery time curves for $\text{CuBi}_2\text{O}_4/x\%\text{PW}_{12}$ at a concentration of 100 ppm formaldehyde.

Table 1 Comparison of CuBi_2O_4 and POMs gas sensors in the literatures

No.	Materials	Morphology	Target gases	Response	Conc. (ppm)	t_{res}/t_{rec} (s)	Temp. (°C)	Ref.
1	$\text{CuBi}_2\text{O}_4/\text{PW}_{12}$	Nanofibers	Formaldehyde	6.68	100	1/2	410	This work
2	CuBi_2O_4	Microparticles	Ethanol	5.9	100	57/294	400	[12]
3	CuBi_2O_4	Nanoparticles	Ethanol	10.8	1000	22/175	400	[13]
4	CuBi_2O_4	Nanospheres/nanoflowers	Formaldehyde	10.9/5.8	60	50/54, 187/106	180	[14]
5	CuBi_2O_4	Microspheres	Formaldehyde	19.1	1000	Not given	240	[15]
6	$\text{CZTS}/\text{PW}_{12}$	Nanoparticles	NO_2	1.8	50	Not given	RT	[37]
7	$\text{SnO}_2@\text{PW}_{12}@\text{WO}_3$	Nanofibers	Ethanol	8.8	100	1/43	280	[40]
8	$\text{MoS}_2@\text{PW}_{12}$	Nanohydrangeas	NO_2	1.61	100	Not given	RT	[17]
9	$\text{TiO}_2@1\%\text{PW}_{12}@\text{MoS}_2$	Nanofibers	Acetone	10.17	100	Not given	300	[18]
10	$\text{PMo}_{10}\text{V}_2@\text{ZIF-8}@\text{ZnO}$	Nanorods	Formaldehyde	5.4	100	15.1/16.2	RT	[41]

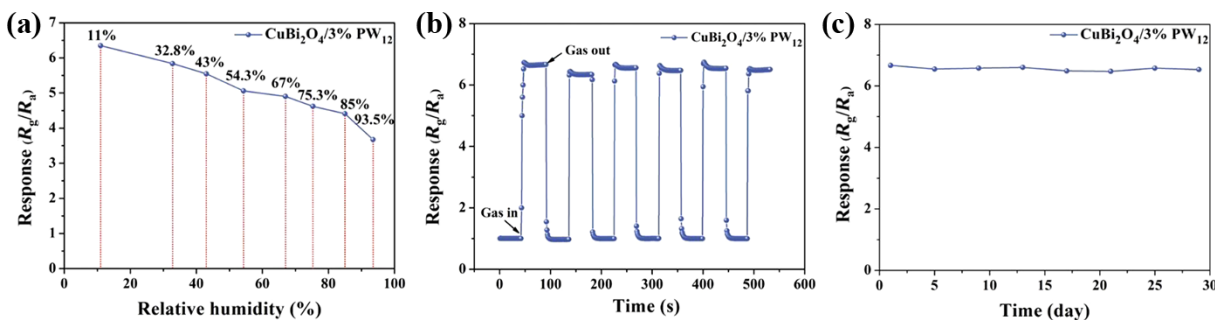


Figure 8 (a) Relative humidity resistance, (b) effect of repeatability, and (c) long-term stability tests of the for $\text{CuBi}_2\text{O}_4/3\%\text{PW}_{12}$ sensor at a concentration of 100 ppm formaldehyde.

with PW_{12} had a lower fluorescence intensity as compared to that of pure CuBi_2O_4 , indicating that stronger fluorescence quenching occurred in $\text{CuBi}_2\text{O}_4/x\%\text{PW}_{12}$. It was observed that PW_{12} as an electron acceptor efficiently inhibited the recombination of electrons in the conduction band of CuBi_2O_4 with holes in the valence band. Due to the introduction of PW_{12} , the carrier

utilization rate and electron mobility of the material improved, and the electron–hole recombination rate reduced. The theory of electron depletion also explained the chemical adsorption of gas molecules in semiconductor gas sensors on the surface of the sensing material, as well as the gas-sensing mechanism of the reaction [32, 33]. As shown in Fig. 10(a), when the $\text{CuBi}_2\text{O}_4/$

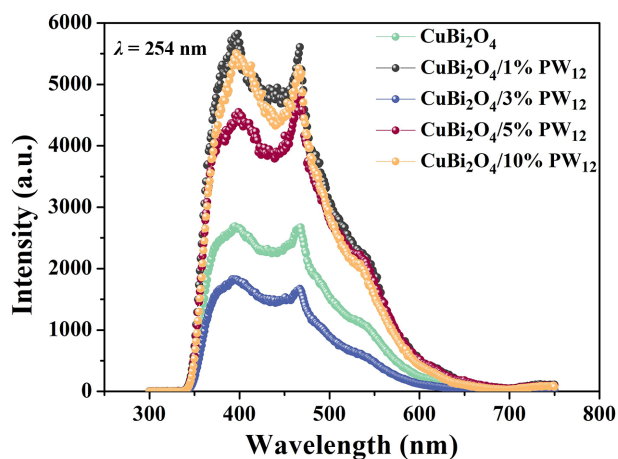
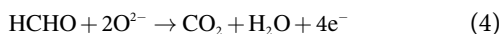
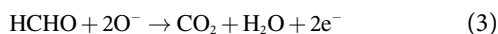
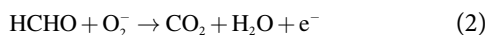


Figure 9 PL spectra of $\text{CuBi}_2\text{O}_4/x\%\text{PW}_{12}$.

$x\%\text{PW}_{12}$ gas sensor was exposed to air, the O_2 adsorbed on the surface of the sensing material captured free electrons from the conduction band of the material, forming a variety of chemically adsorbed oxygen, such as O^{2-} , O^- , and O_2^- [13, 34–37]. The decrease in electrons in the CuBi_2O_4 conduction band caused an electron depletion layer to form on its surface, and since CuBi_2O_4 is a p-type semiconductor, the sensor resistance decreased. When the sensor was exposed to formaldehyde gas, HCHO molecules reacted with various chemo-adsorbed oxygen molecules to form CO_2 and H_2O [4], as shown in the following reactions



At the same time as the reaction occurred, electrons transferred back to the conduction band. Thus, the thickness of the electron depletion layer increased, and the sensor resistance increased. This increase in the sensor resistance led to the improvement of the sensing response of the $\text{CuBi}_2\text{O}_4/x\%\text{PW}_{12}$ sensor. On this basis, it is concluded that PW_{12} as an electron trap can capture electrons to separate them from holes that is, reduce the recombination of electrons, and subsequently improve the response of the sensor. The electron transfer direction is shown in Fig. 10(b). The reduction potential of PW_{12} (+0.23 eV) was observed to be higher than that of CuBi_2O_4 (−0.65 eV), indicating that electrons were transferred from the conduction band of CuBi_2O_4 to the empty d

orbital of PW_{12} [38, 39]. The combination of the electron trap effect of PW_{12} and the p-n heterojunction formed between PW_{12} and CuBi_2O_4 improved the sensor response.

4 Conclusions

In summary, we prepared one-dimensional $\text{CuBi}_2\text{O}_4/x\%\text{PW}_{12}$ nanofibers by using electrospinning technology, and explored the influence of introduction of PW_{12} on the sensing performances of the CuBi_2O_4 gas sensor. Additionally, we studied the sensing mechanism of the $\text{CuBi}_2\text{O}_4/x\%\text{PW}_{12}$ gas sensor. The results showed that the gas sensor introduced with 3% PW_{12} had good repeatability and good stability within 30 days. The $\text{CuBi}_2\text{O}_4/x\%\text{PW}_{12}$ gas sensor response to formaldehyde was found to reach up to 6.68, which was 3.92 times greater than that of the pure CuBi_2O_4 gas sensor. This enhancement was mainly attributed to the property of PW_{12} being an electron acceptor that effectively inhibited the recombination of electrons and holes and improved carrier utilization and electron mobility. Thus, this study contributes novel ideas to the literature regarding the CuBi_2O_4 -based gas sensors and also provides new evidence for the use of POMs to improve the sensing performance of materials.

Electronic Supplementary Material: Supplementary material is available in the online version of this article at <https://doi.org/10.26599/POM.2024.9140053>.

Data availability

All data needed to support the conclusions in the paper are presented in the manuscript. Additional data related to this paper may be requested from the corresponding author upon request.

Acknowledgements

This work was supported by the Jilin Scientific and Technological Development Program (No. YDZJ202101ZYTS032), China Postdoctoral Science Foundation (No. 2023M731268), the National Natural Science Foundation of China (No. 51902029), and Young Elite Scientists Sponsorship Program by CAST (No. 2022QNRC001).

Declaration of competing interest

The authors have no competing interests to declare that are relevant to the content of this article.

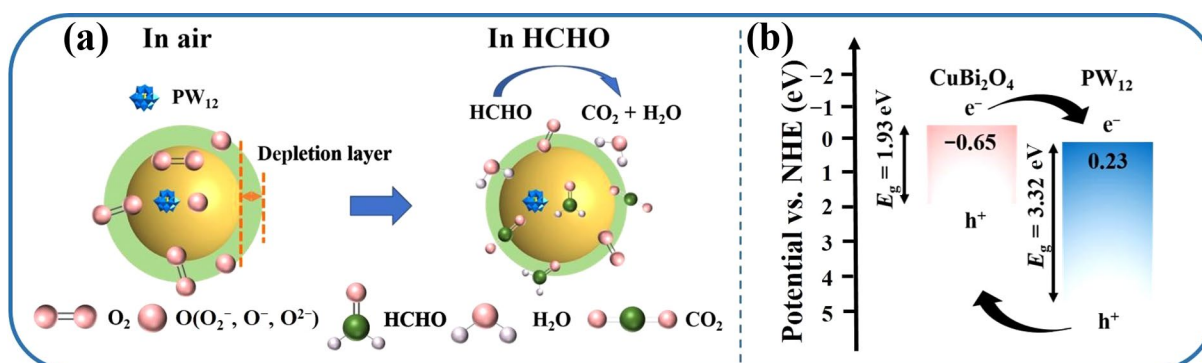


Figure 10 (a) Schematic of the sensing mechanism of $\text{CuBi}_2\text{O}_4/x\%\text{PW}_{12}$ and (b) carrier transfer pathways.

Author contribution statement

Pinfan Song collected the data and wrote the draft; Tianqi Wang contributed to conceived the idea of the study. All authors contributed to the writing and revisions.

References

- [1] Chen, C. X.; Xie, G. Z.; Dai, J.; Li, W. X.; Cai, Y. L.; Li, J.; Zhang, Q. P.; Tai, H. L.; Jiang, Y. D.; Su, Y. J. Integrated core-shell structured smart textiles for active NO₂ concentration and pressure monitoring. *Nano Energy* **2023**, *116*, 108788.
- [2] Su, Y. J.; Liu, Y. L.; Li, W. X.; Xiao, X.; Chen, C. X.; Lu, H. J.; Yuan, Z.; Tai, H. L.; Jiang, Y. D.; Zou, J. et al. Sensing-transducing coupled piezoelectric textiles for self-powered humidity detection and wearable biomonitoring. *Mater. Horiz.* **2023**, *10*, 842–851.
- [3] Pan, H.; Chen, G. R.; Chen, Y. M.; Di Carlo, A.; Mayer, M. A.; Shen, S.; Chen, C. X.; Li, W. X.; Subramaniam, S.; Huang, H. C. et al. Biodegradable cotton fiber-based piezoresistive textiles for wearable biomonitoring. *Biosens. Bioelectron.* **2023**, *222*, 114999.
- [4] Chen, C. X.; Jiang, M. J.; Luo, X. L.; Tai, H. L.; Jiang, Y. D.; Yang, M.; Xie, G. Z.; Su, Y. J. Ni-Co-P hollow nanobricks enabled humidity sensor for respiratory analysis and human-machine interfacing. *Sens. Actuators B: Chem.* **2022**, *370*, 132441.
- [5] Su, Y. J.; Li, W. X.; Cheng, X. X.; Zhou, Y. H.; Yang, S.; Zhang, X.; Chen, C. X.; Yang, T. N.; Pan, H.; Xie, G. Z. et al. High-performance piezoelectric composites via β phase programming. *Nat. Commun.* **2022**, *13*, 4867.
- [6] Wang, T. Q.; Sun, Z. X.; Wang, Y.; Liu, R.; Sun, M. H.; Xu, L. Enhanced photoelectric gas sensing performance of SnO₂ flower-like nanorods modified with polyoxometalate for detection of volatile organic compound at room temperature. *Sens. Actuators B: Chem.* **2017**, *246*, 769–775.
- [7] Zhang, S.; Sun, S. P.; Huang, B. Y.; Wang, N.; Li, X. G. UV-enhanced formaldehyde sensor using hollow In₂O₃@TiO₂ double-layer nanospheres at room temperature. *ACS Appl. Mater. Interfaces* **2023**, *15*, 4329–4342.
- [8] Zhang, B.; Wang, J.; Wei, Q. F.; Yu, P. P.; Zhang, S.; Xu, Y.; Dong, Y.; Ni, Y.; Ao, J. P.; Xia, Y. Visible light-induced room-temperature formaldehyde gas sensor based on porous three-dimensional ZnO nanorod clusters with rich oxygen vacancies. *ACS Omega* **2022**, *7*, 22861–22871.
- [9] Wang, L.; Li, Y.; Yue, W. J.; Gao, S.; Zhang, C. W.; Chen, Z. X. High-performance formaldehyde gas sensor based on Cu-doped Sn₃O₄ hierarchical nanoflowers. *IEEE Sens. J.* **2020**, *20*, 6945–6953.
- [10] Xiao, C. L.; Zhang, X. H.; Ma, Z. Z.; Yang, K.; Gao, X. T.; Wang, H. Q.; Jia, L. C. Formaldehyde gas sensor with 1 ppb detection limit based on In-doped LaFeO₃ porous structure. *Sens. Actuators B: Chem.* **2022**, *371*, 132558.
- [11] Phuoc, P. H.; Van Hoang, N.; Hung, N. M.; Hung, P. T.; Hoat, P. D.; Van Hieu, N. On-chip CuFe₂O₄ nanofiber for conductometric NO₂ and H₂S gas-sensors. *Sens. Actuators B: Chem.* **2023**, *380*, 133306.
- [12] Choi, Y. H.; Kim, D. H.; Hong, S. H. CuBi₂O₄ prepared by the polymerized complex method for gas-sensing applications. *ACS Appl. Mater. Interfaces* **2018**, *10*, 14901–14913.
- [13] Choi, Y. H.; Kim, D. H.; Hong, S. H. Gas sensing properties of p-type CuBi₂O₄ porous nanoparticulate thin film prepared by solution process based on metal-organic decomposition. *Sens. Actuators B: Chem.* **2018**, *268*, 129–135.
- [14] Wang, X.; Liu, W. J.; Wang, C. L.; Zhang, S. W.; Ding, M.; Xu, X. J. Enhanced formaldehyde gas sensing performance of ternary CuBi₂O₄ oxides through oxygen vacancy manipulation and surface platinum decoration. *Sens. Actuators B: Chem.* **2021**, *344*, 130190.
- [15] Xu, J. Z.; Zhang, H. Z.; Fu, Z. M.; Ling, Y. H. Hydrothermal synthesis of hierarchical CuBi₂O₄ microspheres with improved gas sensitivity. *Ceram. Int.* **2022**, *48*, 31519–31527.
- [16] Song, P. F.; Wang, T. Q. Application of polyoxometalates in chemiresistive gas sensors: A review. *ACS Sens.* **2022**, *7*, 3634–3643.
- [17] Wang, P. Y.; Wang, T. Q.; Li, F.; Li, D.; Yang, Y.; Yu, H.; Dong, X. T. Enhanced sensing response of the first polyoxometalate electron acceptor modified MoS₂ for NO₂ gas detection at room temperature. *Sens. Actuators B: Chem.* **2023**, *382*, 133495.
- [18] Wang, P. Y.; Wang, T. Q.; Pei, W. Y.; Li, F.; Yang, Y.; Yu, H.; Dong, X. T. Bi-function of photocatalytic Cr (VI) removal and monitoring acetone gas by one-dimensional hierarchical TiO₂@polyoxometalates@MoS₂ tandem heterojunctions. *Sens. Actuators B: Chem.* **2023**, *387*, 133743.
- [19] Song, J.; Li, Y.; Cao, P.; Jing, X. F.; Faheem, M.; Matsuo, Y.; Zhu, Y. L.; Tian, Y. Y.; Wang, X. H.; Zhu, G. S. Synergic catalysts of polyoxometalate@cationic porous aromatic frameworks: Reciprocal modulation of both capture and conversion materials. *Adv. Mater.* **2019**, *31*, 1902444.
- [20] Lei, J.; Fan, X. X.; Liu, T.; Xu, P.; Hou, Q.; Li, K.; Yuan, R. M.; Zheng, M. S.; Dong, Q. F.; Chen, J. J. Single-dispersed polyoxometalate clusters embedded on multilayer graphene as a bifunctional electrocatalyst for efficient Li-S batteries. *Nat. Commun.* **2022**, *13*, 202.
- [21] Granadeiro, C. M.; Julião, D.; Ribeiro, S. O.; Cunha-Silva, L.; Balula, S. S. Recent advances in lanthanide-coordinated polyoxometalates: From structural overview to functional materials. *Coordin. Chem. Rev.* **2023**, *476*, 214914.
- [22] Amin, S. S.; Jones, K. D.; Kibler, A. J.; Damian, H. A.; Cameron, J. M.; Butler, K. S.; Argent, S. P.; Winslow, M.; Robinson, D.; Mitchell, N. J. et al. Diphosphoryl-functionalized polyoxometalates: Structurally and electronically tunable hybrid molecular materials. *Angew. Chem.* **2023**, *135*, e202302446.
- [23] Xiao, H. P.; Hao, Y. S.; Li, X. X.; Xu, P.; Huang, M. D.; Zheng, S. T. A water-soluble antimony-rich polyoxometalate with broad-spectrum antitumor activities. *Angew. Chem., Int. Ed.* **2022**, *61*, e202210019.
- [24] Chen, J. J.; Vilà-Nadal, L.; Solé-Daura, A.; Chisholm, G.; Minato, T.; Busche, C.; Zhao, T. T.; Kandasamy, B.; Ganin, A. Y.; Smith, R. M. et al. Effective storage of electrons in water by the formation of highly reduced polyoxometalate clusters. *J. Am. Chem. Soc.* **2022**, *144*, 8951–8960.
- [25] Yang, F.; Yu, X. J.; Liu, Z. B.; Niu, J. F.; Zhang, T.; Nie, J. K.; Zhao, N. N.; Li, J. P.; Yao, B. H. Preparation of Z-scheme CuBi₂O₄/Bi₂O₃ nanocomposites using electrospinning and their enhanced photocatalytic performance. *Mater. Today Commun.* **2021**, *26*, 101735.
- [26] Shao, H.; Zhang, Y.; Li, N.; Li, D.; Yu, W. S.; Liu, G. X.; Dong, X. T. One-dimensional LaF₃:RE³⁺ (RE = Eu, Nd) nanostructured phosphors: Controllable synthesis and luminescence properties. *Ceram. Int.* **2023**, *49*, 29094–29103.
- [27] Meng, J. Q.; Wang, X. Y.; Yang, X.; Hu, A.; Guo, Y. H.; Yang, Y. X. Enhanced gas-phase photocatalytic removal of aromatics over direct Z-scheme-dictated H₃PW₁₂O₄₀/g-C₃N₄ film-coated optical fibers. *Appl. Catal. B: Environ.* **2019**, *251*, 168–180.
- [28] Duployer, B.; Tenailleau, C.; Thimont, Y.; Lenormand, P.; Barnabé, A.; Presmanes, L. Preparation and study of CuBi₂O₄ thin films by RF magnetron sputtering. *Mater. Res. Bull.* **2020**, *130*, 110940.
- [29] Li, J.; Xie, G. Z.; Jiang, J.; Liu, Y. Y.; Chen, C. X.; Li, W. X.; Huang, J. L.; Luo, X. L.; Xu, M.; Zhang, Q. P. et al. Enhancing photodegradation of methyl orange by coupling piezo-phototronic effect and localized surface Plasmon resonance. *Nano Energy* **2023**, *108*, 108234.
- [30] Li, H. Y.; Sun, Y. J.; Cai, B.; Gan, S. Y.; Han, D. X.; Niu, L.; Wu, T. S. Hierarchically Z-scheme photocatalyst of Ag@AgCl decorated on BiVO₄ (040) with enhancing photoelectrochemical and photocatalytic performance. *Appl. Catal. B: Environ.* **2015**, *170–171*, 206–214.
- [31] Hong, S. J.; Lee, S.; Jang, J. S.; Lee, J. S. Heterojunction BiVO₄/WO₃

- electrodes for enhanced photoactivity of water oxidation. *Energy Environ. Sci.* **2011**, *4*, 1781–1787.
- [32] Shen, Y. B.; Wang, W.; Chen, X. X.; Zhang, B. Q.; Wei, D. Z.; Gao, S. L.; Cui, B. Y. Nitrogen dioxide sensing using tungsten oxide microspheres with hierarchical nanorod-assembled architectures by a complexing surfactant-mediated hydrothermal route. *J. Mater. Chem. A* **2016**, *4*, 1345–1352.
- [33] Xu, H. Y.; Ju, D. X.; Chen, Z. R.; Han, R.; Zhai, T.; Yu, H. Q.; Liu, C. Y.; Wu, X. W.; Wang, J. Q.; Cao, B. Q. A novel hetero-structure sensor based on Au/Mg-doped TiO₂/SnO₂ nanosheets directly grown on Al₂O₃ ceramic tubes. *Sens. Actuators B: Chem.* **2018**, *273*, 328–335.
- [34] Zhang, C. L.; Wang, J.; Hu, R. J.; Qiao, Q.; Li, X. G. Synthesis and gas sensing properties of porous hierarchical SnO₂ by grapefruit exocarp biotemplate. *Sens. Actuators B: Chem.* **2016**, *222*, 1134–1143.
- [35] Chen, T.; Liu, Q. J.; Zhou, Z. L.; Wang, Y. D. A high sensitivity gas sensor for formaldehyde based on CdO and In₂O₃ doped nanocrystalline SnO₂. *Nano* **2008**, *19*, 095506.
- [36] Suematsu, K.; Uchino, H.; Mizukami, T.; Watanabe, K.; Shimanoe, K. Oxygen adsorption on ZrO₂-loaded SnO₂ gas sensors in humid atmosphere. *J. Mater. Sci.* **2019**, *54*, 3135–3143.
- [37] Yamazoe, N.; Suematsu, K.; Shimanoe, K. Extension of receptor function theory to include two types of adsorbed oxygen for oxide semiconductor gas sensors. *Sens. Actuators B: Chem.* **2012**, *163*, 128–135.
- [38] Wang, Y. T.; Fu, X. Q.; Wang, T. Q.; Li, F.; Li, D.; Yang, Y.; Dong, X. T. Polyoxometalate electron acceptor incorporated improved properties of Cu₂ZnSnS₄-based room temperature NO₂ gas sensor. *Sens. Actuators B: Chem.* **2021**, *348*, 130683.
- [39] Majhi, D.; Mishra, A. K.; Das, K.; Bariki, R.; Mishra, B. G. Plasmonic Ag nanoparticle decorated Bi₂O₃/CuBi₂O₄ photocatalyst for expeditious degradation of 17 α -ethinylestradiol and Cr(VI) reduction: Insight into electron transfer mechanism and enhanced photocatalytic activity. *Chem. Eng. J.* **2021**, *413*, 127506.
- [40] Tian, J. M.; Jiang, B.; Shao, H.; Wang, Y. T.; Wang, T. Q.; Li, F.; Li, D.; Yang, Y.; Dong, X. T. A new strategy to one-step construct polyoxometalate/semiconductor one-dimensional tandem heterojunctions toward optimized conductometric sensing performances of ethanol gas. *Sens. Actuators B: Chem.* **2023**, *374*, 132797.
- [41] Wang, P. Y.; Zou, X. Q.; Tan, H. Q.; Wu, S.; Jiang, L. C.; Zhu, G. S. Ultrathin ZIF-8 film containing polyoxometalate as an enhancer for selective formaldehyde sensing. *J. Mater. Chem. C* **2018**, *6*, 5412–5419.



Tianqi Wang graduated with his first degree in chemistry from Northeast Normal University (NENU) in 2013, and then received his Ph.D. degree (2018) under the direction of Professor Lin Xu from NENU. He worked in Changchun University of Science and Technology in China now. His current research interests focus on polyoxometalate-based multifunctional materials, in particular, polyoxometalates doping in semiconductor materials to improve functional performances, such as photovoltaic devices and gas sensing.



Open Access This article is licensed under a Creative Commons Attribution 4.0 International License (CC BY 4.0), which permits reusers to distribute, remix, adapt, and build upon the material in any medium or format, so long as attribution is given to the original author(s) and the source, provide a link to the license, and indicate if changes were made. See <https://creativecommons.org/licenses/by/4.0/>

© The author(s) 2024. Published by Tsinghua University Press.